Mapping bifurcation structure and parameter dependence in quantum dot spin-VCSELs

NIANQIANG LI,[1,*] H. SUSANTO,[2] B. R. CEMLYN,[1] I. D. HENNING,[1] AND M. J. ADAMS[1]

[1]*School of Computer Science and Electronic Engineering, University of Essex, Wivenhoe Park, Colchester CO4 3SQ, UK*
[2]*Department of Mathematical Sciences, University of Essex, Wivenhoe Park, Colchester CO4 3SQ, UK*
*wan_103301@163.com

Abstract: We consider a modified version of the spin-flip model (SFM) that describes optically pumped quantum dot (QD) spin-polarized vertical-cavity surface-emitting lasers (VCSELs). Maps showing different dynamical regions and those consisting of various key bifurcations are constructed by direct numerical simulations and a numerical path continuation technique, respectively. A comparison between them clarifies the physical mechanism that governs the underlying dynamics as well as routes to chaos in QD spin-VCSELs. Detailed numerical simulations illustrate the role played by the capture rate from wetting layer (WL) to QD ground state, the gain parameter, and the amplitude-phase coupling. By tuning the aforementioned key parameters in turn we show how the dynamical regions evolve as a function of the intensity and polarization of the optical pump, as well as in the plane of the spin relaxation rate and linear birefringence rate, which is of importance in the design of spin lasers promising potential applications. By increasing the capture rate from WL to QD our simulation accurately describes the transition from the QD spin-VCSEL to the quantum well case, in agreement with a previous mathematical derivation, and thus validates the modified SFM equations.

References and links

1. G. H. M. van Tartwijk and D. Lenstra, "Semiconductor lasers with optical injection and feedback," Quantum Semiclass. Opt. **7**(2), 87-143 (1995).
2. M. C. Soriano, J. García-Ojalvo, C. R. Mirasso, and I. Fischer, "Complex photonics: dynamics and applications of delay-coupled semiconductor lasers," Rev. Mod. Phys. **85**(1), 421-470 (2013).
3. M. Sciamanna and K. A. Shore, "Physics and applications of laser diode chaos," Nat. Photonics **9**(3), 151-162 (2015).
4. A. Argyris, D. Syvridis, L. Larger, V. Annovazzi-Lodi, P. Colet, I. Fischer, J. García-Ojalvo, C. R. Mirasso, L. Pesquera, and K. A. Shore, "Chaos-based communications at high bit rates using commercial fibre-optic links," Nature **438**, 343-346 (2005).
5. N. Jiang, C. P. Xue, Y. X. Lv, and K. Qiu, "Physically enhanced secure wavelength division multiplexing chaos communication using multimode semiconductor lasers," Nonlinear Dynamics **86**(3), 1937-1949 (2016).
6. A. Uchida, K. Amano, M. Inoue, K. Hirano, S. Naito, H. Someya, I. Oowada, T. Kurashige, M. Shiki, S. Yoshimori, K. Yoshimura, and P. Davis, "Fast physical random bit generation with chaotic semiconductor lasers," Nat. Photonics **2**(12), 728-732 (2008).
7. X. Z. Li, S. S. Li, and S. C. Chan, "Correlated random bit generation using chaotic semiconductor laser under unidirectional optical injection," IEEE Photon. J. **9**(5), 1505411 (2017).
8. F. Y. Lin and J. M. Liu, "Chaotic lidar," IEEE J. Sel. Topics Quantum Electron. **10**(5), 991-997 (2004).
9. K.H. Lo, S.K. Hwang, and S. Donati, "Numerical study of ultrashort-optical-feedback-enhanced photonic microwave generation using optically injected semiconductor lasers at period-one nonlinear dynamics," Opt. Express **25**(25), 31595-31611 (2017).
10. L. Larger, M. C. Soriano, D. Brunner, L. Appeltant, J. M. Gutierrez, L. Pesquera, C. R. Mirasso, and I. Fischer, "Photonic information processing beyond Turing: an optoelectronic implementation of reservoir computing," Opt. Express **20**(3), 3241-3249 (2012).

11. D. Rontani, D. Choi, C. Y. Chang, A. Locquet and D. S. Citrin, "Compressive sensing with optical chaos," Sci. Rep. **6**, 35206 (2016).

12. L. Jumpertz, K. Schires, M. Carras, M. Sciamanna, and F. Grillot, "Chaotic light at mid-infrared wavelength," Light Sci. Appl. **5**(6), e16088 (2016).

13. H. Han and K. A. Shore, "Dynamics and stability of mutually coupled Nano lasers," IEEE J. Quantum Electron. **52**(11), 2000306 (2016).

14. M. Virte, K. Panajotov, H. Thienpont, and M. Sciamanna, "Deterministic polarization chaos from a laser diode," Nat. Photonics **7**, 60-65 (2013).

15. T. R. Raddo, K. Panajotov, B. H. V. Borges, and M. Virte, "Strain induced polarization chaos in a solitary VCSEL," Sci. Rep. **7**, 14032 (2017).

16. Y. Yu, W. Q. Xue, E. Semenova, K. Yvind, and J. Mørk, "Demonstration of a self-pulsing photonic crystal Fano laser," Nat. Photonics **11**, 81-84 (2017).

17. K. E. Chlouverakis, M. J. Adams, "Stability maps of injection-locked laser diodes using the largest Lyapunov exponent," Opt. Commun. **216**(4), 405-412 (2003).

18. X. X. Guo, S. Y. Xiang, Y. H. Zhang, A. J. Wen, and Y. Hao, "Information-theory-based complexity quantifier for chaotic semiconductor laser with double time delays," IEEE J. Quantum Electron. **54**(1), 2000308, 2018.

19. J. P. Toomey, D. M. Kane, S. Valling, and A. M. Lindberg, "Automated correlation dimension analysis of optically injected solid state lasers," Opt. Exp. **17**(9), 7592-7608 (2009).

20. J. P. Toomey, A. Argyris, C. McMahon, D. Syvridis, and D. M. Kane, "Time-scale independent permutation entropy of a photonic integrated Device," J. Lightw. Technol. **35**(1), 88-95 (2017).

21. S. Valling, T. Fordell, and A. M. Lindberg, "Maps of the dynamics of an optically injected solid-state laser," Phys. Rev. A **72**(3), 033810 (2005).

22. T. B. Simpson, J. M. Liu, K. F. Huang, and K. Tai, "Nonlinear dynamics induced by external optical injection in semiconductor lasers," Quantum Semiclassic. Opt. **9**(5), 765 (1997).

23. A. Valle, M. Sciamanna, K. Panajotov, "Nonlinear dynamics of the polarization of multitransverse mode vertical-cavity surface-emitting lasers under current modulation," Phys. Rev. E **76**, 046206 (2007).

24. C. Schelte, K. Panajotov, M. Tlidi, S. V. Gurevich, "Bifurcation structure of cavity soliton dynamics in a vertical-cavity surface-emitting laser with a saturable absorber and time-delayed feedback," Phys. Rev. A **96**, 023807 (2017).

25. B. Lingnau, W. W Chow, E. Schöll, K. Lüdge, "Feedback and injection locking instabilities in quantum-dot lasers: a microscopically based bifurcation analysis," New J. Phys. **15**, 093031(2013).

26. S. Wieczorek, B. Krauskopf, T. B. Simpson, and D. Lenstra, "The dynamical complexity of optically injected lasers," Phys. Rep. **416**(1), 1-128 (2005).

27. R. Al-Seyab, D. Alexandropoulos, I. D. Henning and M. J. Adams, "Instabilities in spin-polarized vertical-cavity surface-emitting lasers," IEEE Photon. J. **3**(5), 799-809 (2011).

28. N. C. Gerhardt and M. R. Hofmann, "Spin-controlled vertical-cavity surface-emitting lasers," Adv. Opt. Technol. **2012**, 268949 (2012).

29. M. J. Adams and D. Alexandropoulos, "Parametric analysis of spin-polarized VCSELs," IEEE J. Quantum Electron. **45**(6), 744-749 (2009).

30. M. Holub, J. Shin, D. Saha, and P. Bhattacharya, "Electrical spin injection and threshold reduction in a semiconductor laser," Phys. Rev. Lett. **98**(14), 146603 (2007).

31. S. S. Alharthi, A. Hurtado, R. K. Al Seyab, V.-M. Korpijärvi, M. Guina, I. D. Henning, and M. J. Adams, "Control of emitted light polarization in a 1310 nm dilute nitride spin-vertical cavity surface emitting laser subject to circularly polarized optical injection," Appl. Phys. Lett. **105**(18), 181106 (2014).

32. S. S. Alharthi, J. Orchard, E. Clarke, I. D. Henning, and M. J. Adams, "1300 nm optically pumped quantum dot spin vertical external-cavity surface-emitting laser," Appl. Phys. Lett. **107**(15), 151109 (2015).

33. J. Rudolph, D. Hägele, H. M. Gibbs, G. Khitrova, and M. Oestreich, "Laser threshold reduction in a spintronic device," Appl. Phys. Lett. **82**(25), 4516-4518 (2003).

34. D. Basu, D. Saha, and P. Bhattacharya, "Optical polarization modulation and gain anisotropy in an electrically injected spin laser," Phys. Rev. Lett. **102**(9), 093904 (2009); Erratum Phys. Rev. Lett. **102** (12), 129901 (2009).

35. K. Schires, R. K. Al Seyab, A. Hurtado, V.-M. Korpijärvi, M. Guina, I. D. Henning, and M. J. Adams, "Optically-pumped dilute nitride spin-VCSEL," Opt. Express **20**(4), 3550-3555 (2012).

36. H. Susanto, K. Schires, M. J. Adams, and I. D. Henning, "Spin-flip model of spin-polarized vertical-cavity surface-emitting lasers: Asymptotic analysis, numerics, and experiments," Phys. Rev. A **92**(6), 063838 (2015).

37. N. Q. Li, D. Alexandropoulos, I. D. Henning, and M. J. Adams, "Stability analysis of quantum-dot spin-VCSELs," Electronics **5**(4), 83 (2016).

38. N. Q. Li, D. Alexandropoulos, H. Susanto, I. D. Henning, and M. J. Adams, "Quantum dot spin-V (E) CSELs: polarization switching and periodic oscillations," Proc. SPIE **10357**, 103572G (2017).

39. J. Lee, R. Oszwałdowski, C. Gøthgen, and I. Žutić, "Mapping between quantum dot and quantum well lasers: From conventional to spin lasers," Phys. Rev. B **85**, 045314 (2012).

40. A. Gahl, S. Balle, and M. San Miguel, "Polarization dynamics of optically pumped VCSELs," IEEE J. Quantum Electron. **35**(3), 342-351 (1999).

41. M. Lindemann, T. Pusch, R. Michalzik, N. C. Gerhardt, and M. R. Hofmann, "Frequency tuning of polarization oscillations: Toward high-speed spin-lasers," Appl. Phys. Lett. **108**(4), 042404 (2016).

42. M. S. Torre, H. Susanto, N. Q. Li, K. Schires, M. F. Salvide, I. D. Henning, A. Hurtado, and M. J. Adams, "High frequency continuous birefringence-induced oscillations in spin-polarized vertical-cavity surface-emitting lasers," Opt. Lett. **42**(8), 1628-1631 (2017).
43. N. C. Gerhardt, M. Lindemann, T. Pusch, R. Michalzik, and M. R. Hofmann, "High-frequency polarization dynamics in spin-lasers: pushing the limits," Proc. SPIE **10357**, 103572F (2017).
44. P. Bhattacharya, D. Basu, A. Das, and D. Saha, "Quantum dot polarized light sources," Semicond. Sci. Technol. **26**, 014002 (2011).
45. D. Basu, D. Saha, C. C. Wu, M. Holub, Z. Mi, and P. Bhattacharya, "Electrically injected InAs/GaAs quantum dot spin laser operating at 200 K," Appl. Phys. Lett. **92**(9), 091119 (2008).
46. N. Yokota, R. Takeuchi, H. Yasaka, and K. Ikeda, "Lasing polarization characteristics in 1.55- μm spin-injected VCSELs," IEEE Photon. Technol. Lett. 29(9), 711-714 (2017).
47. N. Q. Li, H. Susanto, B. R. Cemlyn, I. D. Henning, and M. J. Adams, "Stability and bifurcation analysis of spin-polarized vertical-cavity surface-emitting lasers," Phys. Rev. A **96**, 013840 (2017).
48. M. J. Adams and D. Alexandropoulos, "Analysis of quantum-dot spin-VCSELs," IEEE Photon. J. **4**(4), 1124-1132 (2012).
49. D. Alexandropoulos, R. Al-Seyab, I. Henning, and M. Adams, "Instabilities in quantum-dot spin-VCSELs," Opt. Lett. **37**(10), 1700-1702 (2012).
50. O. Qasaimeh, "Novel closed-form solution for spin-polarization in quantum dot VCSEL," Opt. Commun. **350**, 83-89 (2015).
51. E. J. Doedel, A. R. Champneys, T. Fairgrieve, Y. Kuznetsov, B. Oldeman, R. Pfaffenroth, B. Sandstede, X. Wang and C. Zhang, AUTO-07p: Continuation and Bifurcation Software for Ordinary Differential Equations (Concordia University, Montreal, 2008).
52. G. A. Gottwald and I. Melbourne, "On the implementation of the 0-1 test for chaos," SIAM J. Appl. Dyn. Syst. **8**(1), 129-145 (2009).
53. M. San Miguel, Q. Feng, and J. V. Moloney, "Light-polarization dynamics in surface-emitting semiconductor lasers," Phys. Rev. A **52**(2), 1728-1739 (1995).
54. H. Erzgräber, S. Wieczorek and B. Krauskopf, "Dynamics of two laterally coupled semiconductor lasers: Strong- and weak-coupling theory," Phys. Rev. E **78**(6), 066201 (2008).
55. N. Q. Li, H. Susanto, B. R. Cemlyn, I. D. Henning, and M. J. Adams, "Locking bandwidth of two laterally-coupled lasers subjected to optical injection," Sci. Rep. **8**(109), 1-10 (2018).
56. N. Q. Li, W. Pan, A. Locquet, and D. S. Citrin, "Time-delay concealment and complexity enhancement of an external-cavity laser through optical injection," Opt. Lett. **40**(19), 4416-4419 (2015).

1. Introduction

Instabilities and nonlinear dynamics in semiconductor lasers, driven by external perturbations, have received considerable attention [1–3], due to their potential applications in chaos-based communications [4, 5], random-number generation [6, 7], chaotic lidar [8], microwave generation [9], reservoir computing [10], and compressive sensing [11]. In recent years, studies of nonlinear dynamics and/or its applications have spread over a wide variety of novel laser structures, including mid-infrared quantum cascade lasers [12], mutually-coupled nanolasers [13], free-running quantum-dot (QD) vertical-cavity surface-emitting lasers (VCSELs) [14], solitary quantum-well (QW) VCSELs with anisotropic strain [15], and photonic crystal Fano lasers [16]. An in-depth understanding of instabilities and nonlinear dynamics is crucial both for uncovering the dominant physical mechanisms from a fundamental point of view, and for locating specific dynamical regimes in the parameter space optimized for the above-mentioned applications. Among many other visualization techniques available to laser dynamics [17–25], bifurcation analysis serves as an efficient means to trace the stability boundaries and clarify the richness of the dynamical behavior, and thus has been widely used in the literature (see [26] and references therein).

Unlike most conventional laser systems, spin-polarized VCSELs can yield various forms of instabilities and even allow for the appearance of chaos [27], without the need of any external perturbation feedback or injection scheme. Early studies of spin-VCSELs have mainly been concerned with continuous wave (cw) operation [28–39], in which interest has centered on superior properties such as threshold reduction and the ease of spin control of the lasing output, compared with their conventional counterparts. Moreover, spin-VCSELs offer faster polarization dynamics oscillating at a frequency mainly determined by the amount of birefringence in the

cavity [40–42] and, in a very recent report, it has been demonstrated that direct modulation frequencies far beyond 100 GHz can be expected through polarization modulation in these lasers [43]. Interest in spin-VCSELs includes the use of either magnetic contacts for electrical injection [34] or carrier generation via optical pumping using circularly polarized light [35], and their implementation with either QW [30, 31, 35] or QD [32, 34, 44, 45] materials. In order to realize their potential gains an understanding of the role of the key parameters is of vital importance. For example, in spin-VCSELs increasing the birefringence in the cavity can lead to the enhancement of frequencies of polarization oscillations [41], e.g., by applying mechanical strain to the VCSEL structure. In contrast, strong birefringence is undesirable for a high degree of circular polarization [29, 46]. In the case of QW spin-VCSELs, understanding instabilities and complicated dynamical behavior has been a topic of intense research. This motivates research on the characterization of dynamics using various approaches, including asymptotic analysis [36], the calculation of the largest Lyapunov exponent (LLE) [27], and bifurcation analysis combining direct numerical simulations and path numerical continuation [47]. In particular, the latter method has provided a full picture of various dynamics accessible to QW spin-VCSELs, and uncovered rich bifurcation scenarios leading to chaos as well as certain auxiliary phenomenon [47], e.g., hysteresis. Surprisingly, little is known about the dynamical instabilities and principal bifurcations that guide the system operation in the case of QD spin-VCSELs. Only limited knowledge of instabilities and effects of some key parameters on the dynamics of QD spin-VCSELs has been provided in a single publication from our group [48], where the LLE method is used as a gauge for the dynamic behavior.

Although at first sight the issue of clarifying various dynamics and their parameter dependence in QD spin-VCSELs might appear to be settled by using the LLE method [48], a closer inspection of the underlying bifurcations unveils the physics governing the dynamics and the important role played by some key parameters in the modified version of the well-known spin-flip model (SFM). For example, bifurcation analysis allows for the identification of the dominant bifurcations occurring at the boundaries of two adjacent dynamical regimes in the parameter space, and the evolution of cw, oscillatory behavior (including period-one (P1), period-two (P2), and even higher periodic states), quasiperiodicity, and chaos as a control/device parameter is varied [26] In this paper, we carry out a systematic study on the bifurcations in QD spin-VCSELs described by a modified version of the SFM equations. Specifically, direct numerical simulations and path numerical continuation methods identify the bifurcations which allow us to provide insight into the physics underlying the various dynamics. High-resolution bifurcation diagrams reveal the role played by some key parameters in each dynamical region mentioned above. Additionally, our method allows us to map out the transition from the QD case to the QW case, further validating the modified SFM equations used throughout this study.

2.   Simulation model

We investigate a model system for an optically pumped spin-polarized VCSEL that incorporates QD gain regions. Based on a QD spin-VCSEL model developed by Adams and Alexandropoulos [48] we use a modified version of the well-known spin-flip model which has been used to study instabilities as well as a form of polarization switching [38], i.e. the sign of the output ellipticity could switch from being the same as that of the ellipticity of the pump, to being of the opposite sign, which successfully reproduces the experimental observations of a 1300nm QD spin vertical external-cavity surface-emitting laser operating at room temperature [32]. The dynamical variables are the normalized conduction band carrier concentrations (n) with subscripts WL (wetting layer) and QD (quantum dot ground state), and superscripts + (spin-down) and − (spin-up), and complex electric fields $\overline{E}_+$ ($\overline{E}_-$) representing right (left) circular polarization (RCP and LCP). Thus, the set of rate equations for the QD spin-VCSEL is given by [37, 38, 48, 49]

$$\frac{d\overline{E}_\pm}{dt} = \kappa \left(n_{QD}^\pm - 1 \right) (1 + i\alpha)\, \overline{E}_\pm - \left(\gamma_a + i\gamma_p \right) \overline{E}_\mp, \tag{1}$$

$$\frac{dn_{WL}^\pm}{dt} = \eta_\pm \gamma_n + h\frac{\gamma_n}{2} - \gamma_o n_{WL}^\pm \left[\frac{h - n_{QD}^\pm}{2h} \right] \mp \gamma_j \left(n_{WL}^+ - n_{WL}^- \right), \tag{2}$$

$$\frac{dn_{QD}^\pm}{dt} = \gamma_o \frac{n_{WL}^\pm}{h} \left(h - n_{QD}^\pm \right) - \gamma_n \left(h + n_{QD}^\pm \right) \mp \gamma_j \left(n_{QD}^+ - n_{QD}^- \right) - 2\gamma_n n_{QD}^\pm \left| \overline{E}_\pm \right|^2. \tag{3}$$

Here, we assume that spin relaxation of carriers within the WL and the QD occurs at the same rate γ_j, the carrier capture rate from WL to QD is denoted by γ_o, and the polarized fields are coupled by the birefringence rate γ_p and also by the dichroism (gain anisotropy) γ_a. To simplify the calculation but still maintain the accuracy, some further assumptions have been made [48,49]: recombination of carriers in the WL is neglected since it is assumed that capture into the ground state of the QD is the dominant process; effects of excited states in the QD are not included (but note that excited states have been included in a development of the model by Qasaimeh [50]), nor are escape of carriers from the QD back to the WL; Pauli blocking of carriers pumped into the WL is neglected, but the blocking effect of capture into the QD is included. The other parameters are the photon decay rate κ, the linewidth enhancement factor α, the right (left) circularly polarized component of the pump η_+ (η_-), the recombination rate of carriers from the QD ground state γ_n, and the normalized gain coefficient as $h = v_g \Gamma a N_D \tau_p$, where v_g is the group velocity, Γ is the optical confinement factor, a is the differential gain, N_D is the density of dots per volume and $\tau_p = (2\kappa)^{-1}$ is the photon lifetime.

The ordinary differential equations given by Eqs. (1)-(3) were numerically integrated with a fourth-order Runge-Kutta method with constant time-step size $\Delta t = 1$ ps. The results are mainly presented in the plane of the pump intensity η ($= \eta_+ + \eta_-$) and pump polarization P ($= (\eta_+ - \eta_-)/(\eta_+ + \eta_-)$). In addition to direct numerical simulations, we carried out a numerical path continuation study and identified the key bifurcations and also mapped them in the (η,P) plane, where the standard continuation package AUTO was used [51]. Due to the symmetric properties present in the system, one has to perform a variable transformation and obtain reduced coordinate equations before using the continuation package AUTO. Following the method introduced in [47], we defined two new variables as

$$\Omega = \left| \overline{E}_+ \right|^2 - \left| \overline{E}_- \right|^2, \tag{4}$$

$$Q = \overline{E}_- \overline{E}_+^*. \tag{5}$$

Rewriting the complex variable Q by using the real/imaginary decomposition $Q = Q_R + iQ_I$, Eq. (1) becomes

$$\frac{d\Omega}{dt} = \kappa \left(n_{QD}^+ + n_{QD}^- - 2 \right)\Omega + \kappa \left(n_{QD}^+ - n_{QD}^- \right)\sqrt{\Omega^2 + 4\left|Q\right|^2} + 4\gamma_p Q_I, \tag{6}$$

$$\frac{dQ_R}{dt} = \kappa \left(n_{QD}^+ - 1 \right)(Q_R + \alpha Q_I) + \kappa \left(n_{QD}^- - 1 \right)(Q_R - \alpha Q_I) - \gamma_a \sqrt{\Omega^2 + 4\left|Q\right|^2}, \tag{7}$$

$$\frac{dQ_I}{dt} = \kappa \left(n_{QD}^+ - 1 \right)(Q_I - \alpha Q_R) + \kappa \left(n_{QD}^- - 1 \right)(Q_I + \alpha Q_R) - \gamma_p \Omega. \tag{8}$$

Equations (2), (3), (6)-(8) can be implemented and numerically solved in the continuation package AUTO, which allows tracking of the stable or unstable steady-state and periodic solutions

and detection of various bifurcations. It is worth noting that $|\overline{E}_+|^2$ and $|\overline{E}_-|^2$ in Eq. (3) can be written as $0.5(\Omega + \sqrt{\Omega^2 + 4|Q|^2})$ and $0.5(-\Omega + \sqrt{\Omega^2 + 4|Q|^2})$, respectively.

Unless specified otherwise, all the numerical simulations were performed with a basic set of parameters which are similar to those already been used in previous works [37, 48]: $\kappa = 250$ ns^{-1}, $\alpha = 3$, $h = 1.1995$, $\gamma_o = 400$ ns^{-1}, $\gamma_j = 10$ ns^{-1}, $\gamma_p = 20$ ns^{-1}, $\gamma_a = 0$ ns^{-1}, and $\gamma_n = 1$ ns^{-1}. We would like to point out that, since the results computed from RCP and LCP components are exactly the same, only those for the RCP component are presented.

3. Results and discussion

Before studying the various bifurcations, we first discuss how a QD spin-VCSEL loses stability from cw operation as one control parameter is varied. Since we consider optical excitation as the means of spin injection, there exist two fully controllable parameters, i.e., pump intensity η and pump polarization P. Following the method presented earlier, we carried out a stability analysis of the steady-state solutions of Eqs. (1)-(3). It has been demonstrated that the modified SFM allows the existence of two types of equilibrium, i.e. in-phase and out-of-phase, depending on the phase difference according to the "continuation" of 0 or π [37].
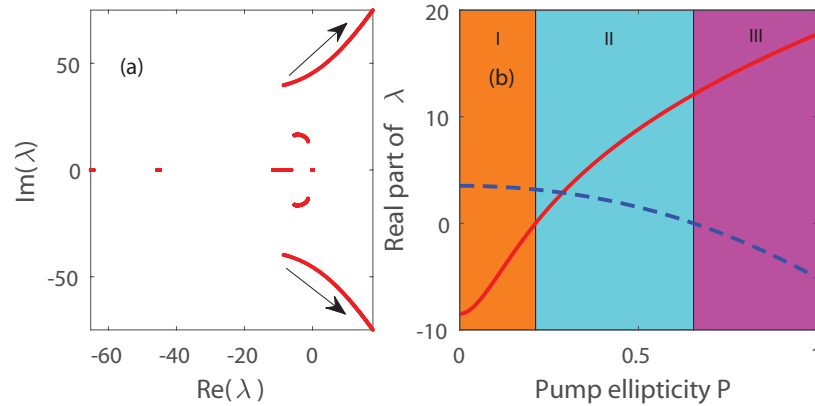

Fig. 1. (a) The eigenvalues λ of the in-phase solution in the complex plane as P increases from 0 to 1, with the trajectory direction of the critical eigenvalues λ indicated by the arrows. (b) The real parts of the critical eigenvalues λ for the in-phase (with positive slope) and out-of-phase (negative slope) solution as a function of P. In both panels, $\eta = 1.5$.

Figure 1(a) shows the eigenvalues λ responsible for the in-phase solution in the complex plane for $\eta = 1.5$. They were calculated from the coefficient matrix in Eq. (9) presented in [37] when the pump polarization is gradually changed from linear ($P = 0$) to right circular ($P = 1$). From this figure we can observe a strong P dependence of the stability of the in-phase solution. Increasing P leads to destabilize the in-phase solution as the real parts of the pair of eigenvalues become positive (indicated by arrows). This also implies that the in-phase solution is destabilizing through a supercritical Hopf bifurcation as a pair of complex conjugate eigenvalues crosses the complex plane imaginary axis. The results for the eigenvalues λ of the out-of-phase solution in the complex plane are not shown, but it is worth noting that the effect of P on the out-of-phase solution is stabilizing it, opposite to the in-phase case. This can be confirmed by comparing the evolution of the critical eigenvalue in both cases, as shown in Fig. 1(b). It is clear that the in-phase solution and the out-of-phase solution are stable in region I and region III, respectively, whereas in region II both solutions are unstable, probably giving rise to oscillatory behavior and even chaos. Hence, crossing the boundary between regions I and II or regions II and III

indicates that the system undergoes a supercritical Hopf bifurcation, which forms the instability threshold. That is, at the critical value of the control parameter, the stationary solutions would destabilize to time-periodic or more complicated dynamics. A bifurcation diagram obtained from direct numerical simulations allows us to see more clearly the instability threshold and further bifurcation scenarios leading to complicated dynamics.
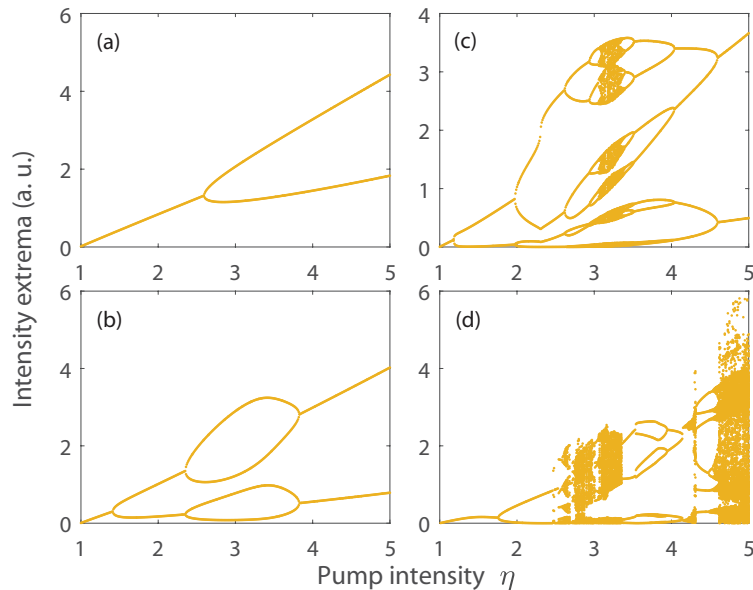

Fig. 2. Bifurcation diagram with η as the control parameter calculated for (a) $P = 1$, (b) $P = 0.6$, (c) $P = 0.4$, and (d) $P = 0.1$. In all panels, the extrema (maxima and minima) of the intensity time series are shown as dots. Other parameters are the same as those given at the end of section 2.

Some representative examples of one-parameter bifurcation diagrams are shown in Fig. 2, where successive extrema (maxima and minima) of the laser intensity as a function of η are plotted for different values of P. In all cases, the system becomes unstable through a Hopf bifurcation, representing the instability threshold, and yields periodic oscillations or even more complicated intensity waveforms if further bifurcations continue. These confirm the results in Fig. 1 which correspond to the time-independent prediction. Some other important features should be emphasized. For large P, roughly $P \geq 0.4$ shown in Figs. 2(a)-2(c), the system output is dominated by the out-of-phase stationary solution before crossing the instability threshold , while for small P, the system operates in the cw determined by the in-phase stationary solution instead [see Fig. 2(d) for $P = 0.1$]. Actually, these have also been predicted in Fig. 1. In Figs. 2(b) and 2(c), our laser exhibits period-doubling dynamics in the first part of increasing η and especially in Fig. 2(c), a common period-doubling route to chaos is clearly observed. In contrast, the laser may become chaotic through the break-up of a torus, resembling a quasiperiodic route to chaos, as shown in Fig. 2(d). It is interesting to find that the QD spin-VCSELs allow for these two bifurcation scenarios leading to chaos, which have also been identified in the case of QW spin-VCSELs [47].

For the results considered so far only one control parameter was varied. We next examine the instability threshold of the system in the (η, P) plane. This is important since it provides information about the boundary between stability and instability in the parameter space. To this end, we used the continuation package AUTO, with which bifurcations can be detected and

followed in parameter space. As indicated in [48], two important parameters are the capture rate from WL to QD ground state γ_o and the gain parameter h, which are specific to QD spin-VCSELs. For this reason it is of interest to check the dependence of the instability threshold on these two parameters.

In Fig. 3 we show the two-parameter continuation of the Hopf bifurcations H_1 (arising from the out-of-phase solution) and H_2 (from the in-phase solution). From this figure we observe that two instability boundaries in the (η,P) plane. To the right of the H_1 boundary we see the time-periodic or even more complicated dynamics, to the left cw operation. A similar result is seen with the H_2 boundary. This figure also shows that the value of both parameters plays an important role in the instability threshold. More specifically, increasing γ_o or h greatly shrinks the size of the instability region, even though the upper limit (H_1) and lower limit (H_2) move oppositely as indicated by arrows as the parameter is increased. In fact, some preliminary evidence for the suppression of the region of instability through increasing one of these two parameters was seen using the LLE method [48], but here bifurcation analysis provides further insight into the physics underlying the shrinkage.
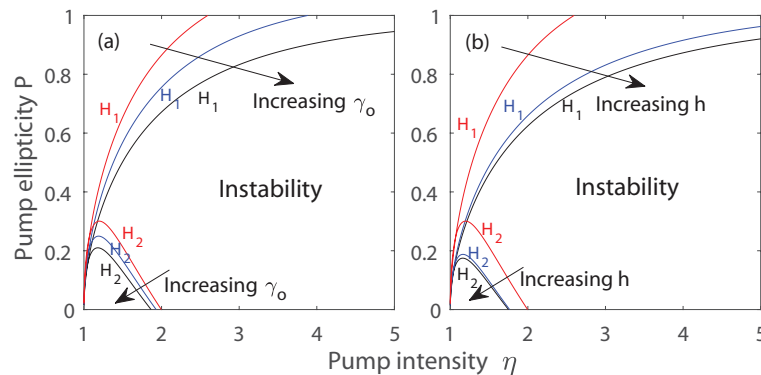

Fig. 3. Bifurcation diagrams for the Hopf bifurcation (instability threshold) in the (η,P) plane. In (a), three values of γ_o are considered: $\gamma_o = 400$ ns^{-1}, 600 ns^{-1}, and 1000 ns^{-1}, and $h = 1.1995$. In (b), three values of h are considered: $h = 1.1995$, 2 and 4, and $\gamma_o = 400$ ns^{-1}. In both panels, the upper limit (H_1) occurs on the branch of the out-of-phase solution, while the lower limit (H_2) stems from the in-phase solution. Other parameters are the same as those given at the end of section 2.

In addition to the Hopf bifurcation which accounts for the instability threshold, we now consider further bifurcations including period-doubling, saddle node of limit cycle and torus, which are of particular importance for finding the locations of more complex dynamics and chaos. Figures 4(a) and 4(b) display two-parameter bifurcation diagrams in the (η,P) plane for wetting layer capture rates $\gamma_o = 400$ ns^{-1} and 600 ns^{-1}, respectively. Only bifurcations forming the backbone of the underlying dynamics are shown to keep the figure simple. In particular, a web of curves for Hopf (H), period-doubling (PD^1,PD^2), torus (TR), and saddle-node of limit cycles (LPC) is illustrated in these figures. Here PD^1 and PD^2 denote two successive period doublings of a limit cycle of basic period. Higher period-doubling curves are not followed since PD^2 curves already provide adequate information on locating chaos [47]. However, they should lie inside each other (i.e. similar to the relation between PD^1 and PD^2) and accumulate according to Feigenbaum's universal scaling law [26], and their discussion is beyond the scope of this work. The comparison of Figs. 4(a) and 4(b) shows that the overall structure of the bifurcation remains unchanged despite the fact that the region allowing oscillatory excitation shrinks in size, bifurcation curves shift slightly, and differ slightly in their appearance as the capture rate

is increased. This situation holds for a wide range of γ_o , but the detailed discussion about the range is not the main focus of the current article.

Two-parameter bifurcation diagrams can also be obtained with the aid of direct numerical simulations of the rate equations. Specifically, the different dynamical regimes are identified from the extrema (maxima and minima) of the intensity time traces, in which cw, P1, P2, and complex dynamics are identified as a constant intensity, two intensity extrema, four intensity extrema, and even more extrema, respectively. Following the definition in [47], the cw, P1, and P2 are marked in purple, blue, and cyan, respectively, while other colors are used to represent complicated dynamics including chaos where the number of extrema exceeds 4 and gradually increases using green to yellow, red, and dark red. In Figs. 4(c) and 4(d) we present such bifurcation maps for $\gamma_o = 400$ ns^{-1} and 600 ns^{-1} in the parameter space consistent with that in Figs. 4(a) and 4(b). A comparison between Figs. 4(c) and 4(d) indicates that the complicated dynamical region is greatly expanded, but only limited to that confined by the P2 region. That means that increasing the capture rate is indeed beneficial to have a wider region of complex dynamics and chaos. Furthermore, comparison with Figs. 4(a) and 4(b) shows that the current bifurcation analysis uncovers various boundaries of complex dynamical regions, including higher period-doubling curves, torus curves, as well as curves representing saddle-node of limit cycles. This kind of information cannot be extracted by using the LLE method [48]. In addition, our two-parameter bifurcation diagrams also unveil different bifurcation routes to chaos, depending on from which side the maps are entered. For instance, it is possible to encounter quasiperiodic oscillations and then chaos by crossing the maps from left to right at low values of P, roughly $P \leq 0.1$; otherwise, bifurcation scenarios are associated with a period-doubling route to chaos.

It should be note that in Figs. 4(c) and 4(d), the number of intensity extrema was used to distinguish different dynamic regions; however, a large value of this measure does not necessarily indicate chaotic emission. For this reason, we employ the 0-1 test for chaos to separate chaotic emission from nonchaotic emission [52]. This calculation is fast and easy to implement and interpret, giving a result of 1 for chaos and 0 for other dynamics. The results of this 0-1 test are illustrated in Figs. 4(e) and 4(f), corresponding to $\gamma_o = 400$ ns^{-1} and 600 ns^{-1}, respectively. Comparison with mapping results in Figs. 4(c) and 4(d) shows that the regions of complicated dynamics identified via our bifurcation analysis overlap with those obtained from the 0-1 test for chaos, indicating that our method to calculate high-resolution bifurcation diagrams provides a very precise prediction of chaos. This also coincides with the LLE calculation. For this reason, in what follows we rely solely on the high-resolution bifurcation maps consisting of the directly simulated dynamical regions to address the influence of key parameters on the dynamics.

Next we investigate whether the transition from QD to QW occurs as we approach the limit when the capture of carriers from the WL to GS is instantaneous, i.e., $\gamma_o \rightarrow \infty$, which was predicted by taking the limit of the QD SFM equations, but was not attempted by estimation of the LLE [48]. In order to investigate the existence of such possible transition numerically, we increased the capture rate γ_o to 7000 ns^{-1}, an order of magnitude larger than expected values. The resulting bifurcation diagram is illustrated in Fig. 5(a). When compared to Figs. 4(c) and 4(d), one can see that the upper limit of the oscillatory region is remarkably compressed and the P2 region (cyan) greatly shrinks; however, the regions corresponding to more complex dynamics and chaos are dramatically expanded and finally merge together, clearly different than the case for smaller capture rates, where separate islands of complex dynamical regions were seen. Fig. 5(b) shows the bifurcation diagram obtained from the SFM of the QW spin-VCSELs and using the same parameters as in Fig. 5(a), except for the 'effective' spin relaxation rate $\gamma_s = \gamma_n + 2\gamma_j$ as defined in [53]. Not surprisingly, the two bifurcation diagrams are in excellent agreement with each other, both for the various dynamical regions and the bifurcation boundaries. Thus result shown in Fig. 5 suggest that given suitable parameters our bifurcation analysis permits a detailed comparison between the SFM for the QD spin-VCSEL and that for the QW case.
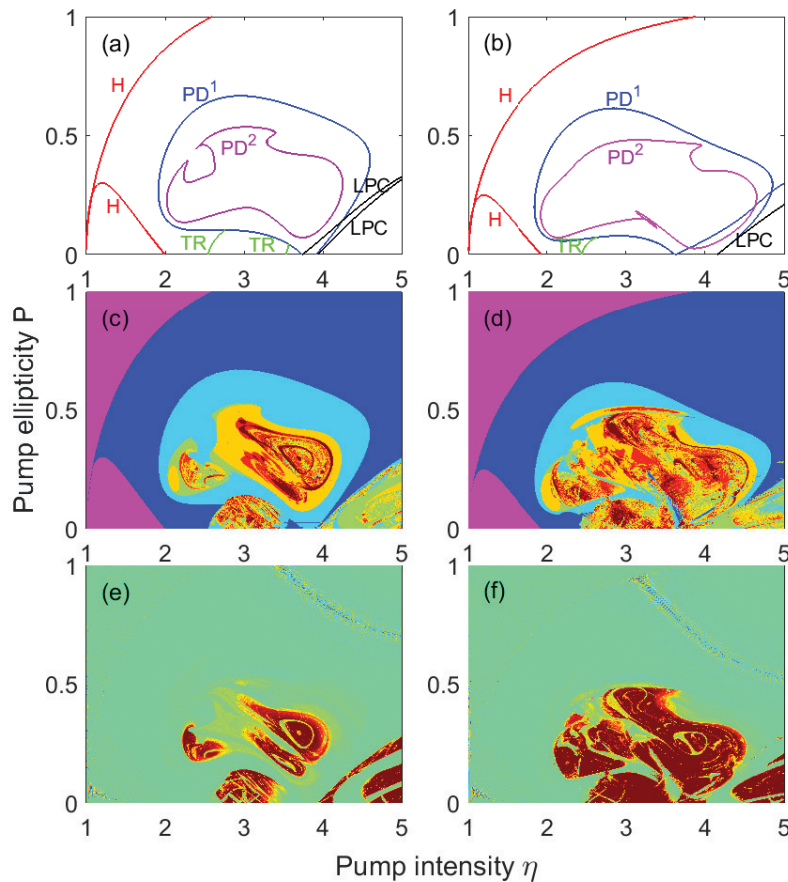
Fig. 4. Bifurcation diagrams obtained by using the package AUTO and (c,d) obtained from direct numerical simulations and represented in colors in the (η,P) plane. (e,f) maps obtained by using the 0-1 test for chaos. Left: $\gamma_o = 400$ ns^{-1}; right: $\gamma_o = 600$ ns^{-1}. In (c,d), purple stands for cw, blue for P1, cyan for P2, and other colors for complicated dynamics. In (e,f), red for chaos, and others for nonchaotic states. Other parameters are the same as those given at the end of section 2.

As becomes evident from Fig. 2, the stability properties of the QD spin-VCSEL also strongly depend on the important gain parameter h. Furthermore, Fig. 4 in [48] indicates that increasing h results in the enhancement of chaotic region and the whole unstable region contracts. However, it remains unclear what would take place at relatively high values of h. To this end, we generate two-parameter bifurcation diagrams using a wider range of h values. For illustrative purposes, the results for two different but fixed values of h are shown in Fig. 6. A comparison between Fig. 6(a) ($h = 2$) and Fig. 4(c) ($h = 1.1995$) shows that chaos is indeed enhanced to some extent with increasing h, consistent with the observation based on the LLE method. As h further increases, roughly above 4, the boundaries (bifurcations) and the underlying dynamics in each region in the parameter space remain unchanged, independent of the exact value of h. One example is displayed in Fig. 6(b), where $h = 10$. The parameter h combines the key fundamental quantities determining laser threshold, namely the maximum optical gain per unit length if all QD ground states were occupied, $\Gamma a N_D$, and the photon lifetime, τ_p. The normalization of the carrier densities includes h in such a way that $h > 1$ is required for lasing when the QD ground states
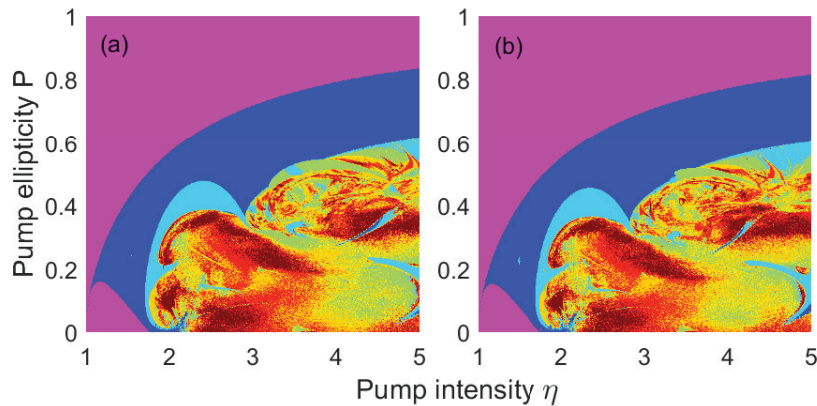
Fig. 5. Bifurcation diagrams obtained from direct numerical simulations and represented in colors in the (η,P) plane for (a) the QD spin-VCSEL with $\gamma_o = 7000$ ns^{-1} and (b) the QW spin-VCSEL. Other parameters are the same as those given at the end of section 2 and color codes are the same as in Fig. 4.
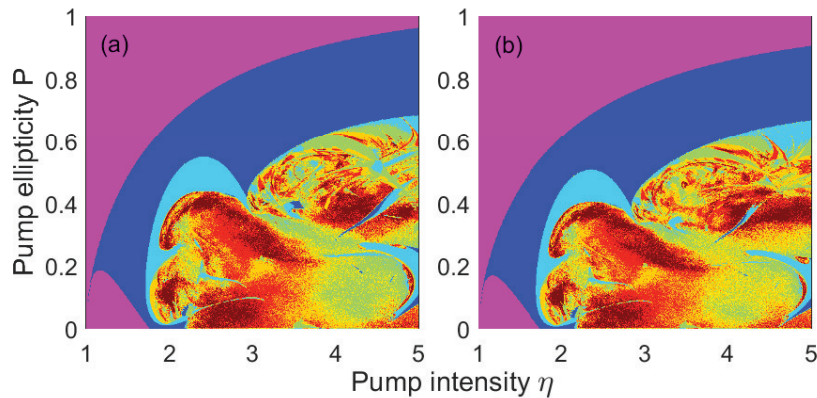

Fig. 6. Bifurcation diagrams obtained from direct numerical simulations and represented in colors in the (η,P) plane for (a) $h = 2$ and (b) 10. Other parameters are the same as those given at the end of section 2 and color codes are the same as in Fig. 4.

are populated by capture of carriers from the wetting layer. This condition would be ensured by suitable cavity and material design, but beyond this there is freedom to increase h if this is beneficial for other design considerations. Thus h can be used as a guide to the resultant nonlinear dynamic behavior, to identify the narrow design range over which some engineering control of the stability characteristics is possible, or for large h to specify the fixed regions of dynamics.

The two parameters just described are specific to the QD spin-VCSEL. In a broader context, it is of interest to study the influence of other parameters that are also present in conventional VCSELs on the lasing dynamics using high-resolution bifurcation diagrams. For illustrative purposes, we now focus on two other important parameters in the SFM, viz. the spin relaxation rate γ_j and the birefringence rate γ_p. Figures 7(a)-7(c) present the results in the (γ_j,γ_P) plane for three different values of P with $\eta = 3$. For large P ($P = 1$), cw emission and P1 oscillations are only seen in the (γ_j,γ_P) plane using the basic set of parameters we have chosen [see Fig. 7(a)]. As P is reduced ($P = 0.6$), a small portion of regions corresponding to P2 and higher-periodic
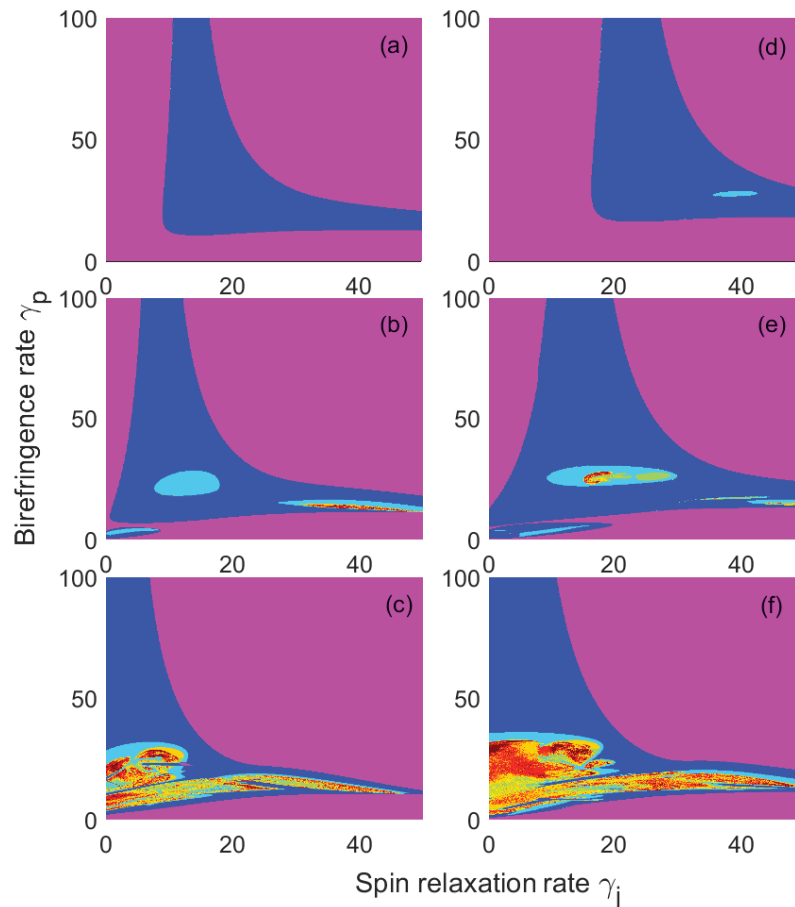
Fig. 7. Bifurcation diagrams obtained from direct numerical simulations and represented in colors in the (γ_j, γ_p) plane for (a-c) $h = 1.1995$ and (d-f) 2, where (a,d) $P = 1$, (b,e) 0.6, and (c,f) 0.2. In all panels $\eta = 3$. Other parameters are the same as those given at the end of section 2 and color codes are the same as in Fig. 4.

oscillations or other irregular dynamics arises [see Fig. 7(b)]. For even smaller values of P, e.g. $P = 0.2$, the system allows for complicated dynamics and chaos as evidenced from the bifurcation diagram shown in Fig. 7(c). In all cases, the oscillatory region resembles the letter L, so we call this L-shaped region. As can be seen from the figure, the L-shaped region is confined by the Hopf bifurcation boundaries and, is shifted to the left of the bifurcation map (the location of smaller γ_j) as P is decreased. A closer inspection of these results indicates that smaller values of γ_j, γ_P, and P are desirable to find more complicated dynamics in the QD spin-VCSEL. Taking into account the generality of these findings, we considered the case of a slightly higher gain parameter $h = 2$ and the corresponding results are shown in Figs. 7(d)-7(f). Similarly, we see the appearance of the L-shaped region, its tunability versus P, and the existence of complicated dynamics on basis of small values of γ_j, γ_P, and P. These results suggest that this is a generic feature of the lasing dynamics in the QD spin-VCSEL.

Finally, we consider another important parameter, i.e., the linewidth enhancement factor α, accounting for the amplitude-phase coupling, which has been widely studied in various laser configurations in the literature [26, 54–56]. We use our same basic set of parameters in Fig. 8(a),
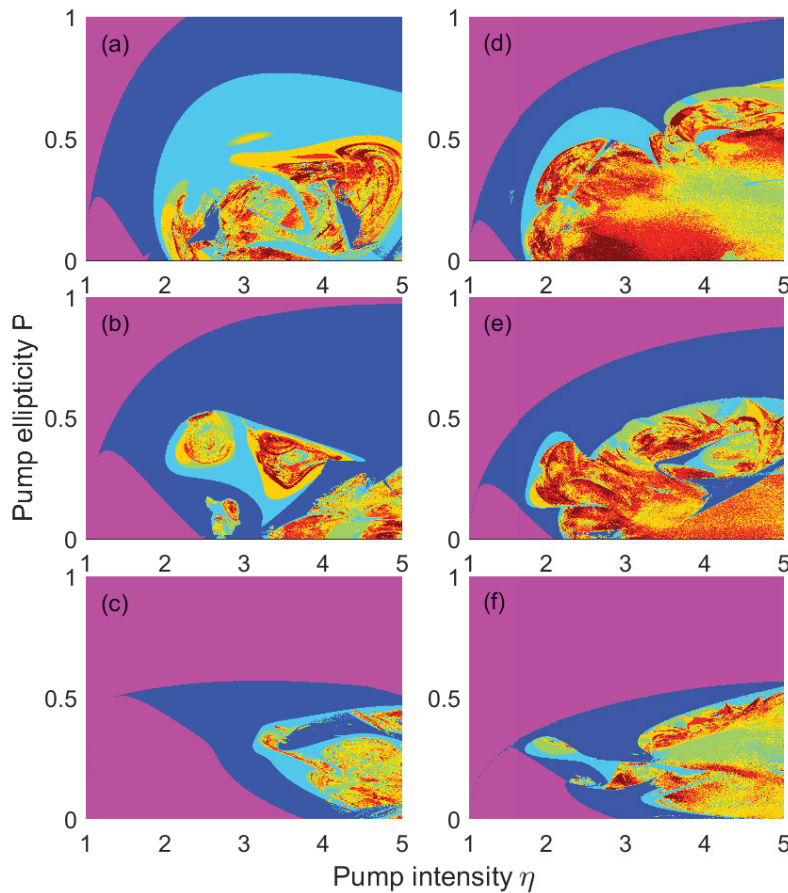
Fig. 8. Bifurcation diagrams obtained from direct numerical simulations and represented in colors in the (η, P) plane for (a-c) $h = 1.1995$ and (d-f) 2, where (a,d) $\alpha = 4$, (b,e) 2, and (c,f) 1. Other parameters are the same as those given at the end of section 2 and color codes are the same as in Fig. 4.

except for a slightly larger linewidth enhancement factor ($\alpha = 4$). We find P2 and other irregular dynamics are enhanced and their regions are greatly expanded when compared to Fig. 4(c) for $\alpha = 3$. This is an expected feature since increasing α enhances amplitude-phase coupling effects, which is a driving force for complicated dynamics. In contrast as the linewidth enhancement factor is slightly reduced ($\alpha = 2$), the whole instability region is suppressed to some extent, and notably the regions of P2 and more complex dynamics dramatically shrink in size; see Fig. 8(b). For an even smaller value ($\alpha = 1$), the whole oscillatory region bounded by two Hopf bifurcation curves shrinks remarkably, as shown in Fig. 8(c). We would like to point out that when $\alpha = 0$ the laser operates in cw emission in the whole parameter space for the parameter values considered (not shown here). For the same purpose as in Fig. 7, we here also considered the case of $h = 2$. The results are depicted in Figs. 8(d)-8(f). Once again, with the help of the high-resolution bifurcation diagrams, we clearly see that increasing α leads to the enhancement of complicated dynamical regions, while decreasing α tends to stabilize the output emission in the QD spin-VCSEL.

4. Conclusion

In conclusion, we have analyzed dynamical properties of the QD spin-VCSEL, which is described by a modified version of the well-known SFM. To the best of our knowledge, we have presented the first demonstration of various bifurcation structures in this specific laser system, which is essentially important for gaining insight into the physics from the fundamental point of view as well as finding specified dynamical regions supporting various potential applications. In particular, we have combined the direct numerical simulations and path numerical continuation methods and mapped out the dynamical regimes including cw, periodic and chaos mainly in the pump intensity and polarization space as well as in the plane of the spin relaxation rate and the birefringence rate. In particular we highlight and discuss the influence of key parameters of the dynamic behavior of spin VCSELs, including the capture rate from the WL to the QD, the gain parameter, the spin relaxation rate, the birefringence rate, and the linewidth enhancement factor. Moreover, our bifurcation analysis has also allowed for the comparison between the QW and QD case, where a smooth transition from the QD case to the QW case was clearly observed by choosing the limiting case when the capture of carriers from the WL to the QD becomes instantaneous. As such, compared to our previous report using an LLE calculation [48], the current study provides a more comprehensive understanding of the rich dynamics, the bifurcations, and their parameter dependence in the QD spin-VCSEL. Moreover, as QD technology matures it reveals the potential via the additional degrees of freedom in QD VCSELs for controlling the dynamic characteristics.